nature geoscience

Brief Communication

https://doi.org/10.1038/s41561-024-01406-4

Production of Neoproterozoic banded iron formations in a partially ice-covered ocean

Received: 16 May 2023

Accepted: 16 February 2024

Published online: 9 April 2024

Check for updates

Kaushal Gianchandani [1] ✉, Itay Halevy [2] ✉, Hezi Gildor [1], Yosef Ashkenazy [3] & Eli Tziperman [4]

The meridional extent of marine ice during the Neoproterozoic snowball Earth events is debated. Banded iron formations associated with the Sturtian glaciation are considered evidence for a completely ice-covered, ferruginous ocean (hard snowball). Here, using an ocean general circulation model with thick sea glaciers and Neoproterozoic biogeochemistry, we find that circulation in a partially ice-covered ocean (soft snowball) yields iron deposition patterns similar to the observed distribution of Sturtian banded iron formations.

Banded iron formations (BIFs) are iron- and silica-rich sedimentary rocks, the genesis of which is thought to require low oceanic O_2 concentrations, in agreement with their occurrence before ~1,800 million years ago (Ma), when Earth's oceans are proposed to have been anoxic[1,2]. An exception to this pattern of occurrence, Neoproterozoic (1,000 to 541 Ma) iron formations, were deposited when atmospheric O_2 levels were 1–10% of today's[3]. Neoproterozoic BIFs occur in association with the Sturtian pan-glacial, which is the earlier and longer of two low-latitude glaciations (the 'snowball Earth' events[4–7]). The ocean and continents are suggested to have been ice-covered during these pan-glacials that lasted for tens of millions of years[8,9]. Widespread sedimentary and geochemical evidence supports the occurrence of the Neoproterozoic pan-glacials, though the meridional extent of marine ice is still debated. The Neoproterozoic BIFs have historically been suggested to support a 'hard' snowball[4,5], in which pole-to-pole ice cover renders the ocean anoxic, allowing the accumulation of ferrous iron (Fe^{2+}). Although viable explanations for the survival of the photosynthesis-based marine biosphere through a hard snowball have been proposed[10], such an extreme climate poses a serious challenge to life[5]. Alternatively, a 'soft' snowball[7] with tropical swaths of open water does not pose a similar challenge to the biosphere, but O_2 input to the ocean by air–sea gas exchange may have prevented the mobility of Fe^{2+} required for widespread deposition of BIFs[10,11].

In this study, we tested the sensitivity of precipitation of BIFs to the extent of ice cover using an ocean general circulation model (GCM), which includes the representation of thick sea glaciers extending to a prescribed latitude and a new biogeochemical model tailored to the Neoproterozoic (Fig. 1; see Methods for details). In the model iron cycle, a hydrothermal source of Fe^{2+} at mid-oceanic ridges is balanced by oxidation and deposition of ferric iron (Fe^{3+}) oxides, which occurs where Fe^{2+}-bearing waters meet oxygenated waters. The transport of Fe^{2+} and O_2 from their respective hydrothermal and photosynthetic sources determines the location of such reaction and deposition fronts. Note that photosynthesis and O_2 production in the partially glaciated oceans that we simulate is confined to the ice-free regions and there is no primary production beneath the >100-m-thick sea glaciers. Patterns of phosphate concentration ($[PO_4^{3-}]$) and $[O_2]$ obtained in an idealized model configuration (Supplementary Section 1) with a 100% modern $[PO_4^{3-}]$ and a stoichiometry of organic matter oxidation (O_2 consumed to P released) representative of modern marine organic matter are consistent with today's ocean (Supplementary Fig. 1), and atmospheric O_2 stabilizes at ~62% present atmospheric levels.

Previous ocean–atmosphere–cryosphere modelling efforts have identified multiple stable climate states in which ice-free ocean exists equatorwards of latitudes between 60° and 5° (refs. 11,12). However, not many climate models can sustain a narrow equatorial band of ice-free ocean. Accordingly, we examined a completely ice-free ocean and partially glaciated oceans in which the ice-free region extended from 30° S to 30° N and 12° S to 12° N. The exact size of the marine PO_4^{3-} pool during snowball Earth episodes is unknown, though several factors lead to expectations of lower-than-present seawater $[PO_4^{3-}]$. These include low continental weathering rates, photosynthetic carbon fixation and

[1]Fredy & Nadine Herrmann Institute of Earth Sciences, Hebrew University of Jerusalem, Jerusalem, Israel. [2]Department of Earth and Planetary Sciences, Weizmann Institute of Science, Rehovot, Israel. [3]Department of Solar Energy and Environmental Physics, Blaustein Institutes for Desert Research, Ben-Gurion University of the Negev, Midreshet Ben-Gurion, Israel. [4]Department of Earth and Planetary Sciences and School of Engineering and Applied Sciences, Harvard University, Cambridge, MA, USA. ✉e-mail: kaushal.g@mail.huji.ac.il; itay.halevy@weizmann.ac.il

https://doi.org/10.1038/s41561-024-01406-4

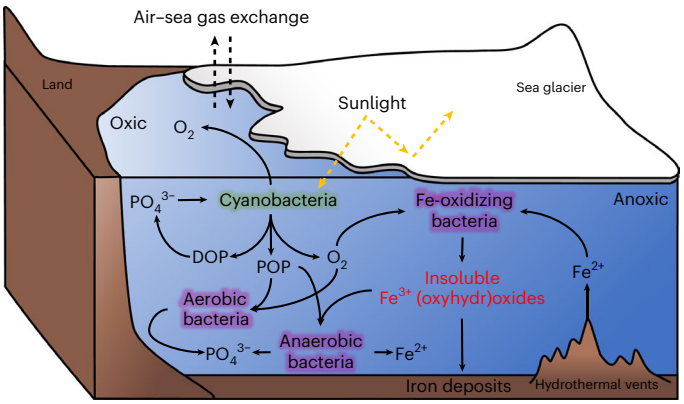

Fig. 1 | Schematic representation of the biogeochemical model. Cyanobacteria, limited by low seawater phosphate concentration ($[PO_4^{3-}]$), produce organic matter (DOP and POP) and oxygen (O_2) in ice-free regions. Aerobic respiration of the organic matter consumes some of the O_2, as do the bacteria that oxidize ferrous iron (Fe^{2+}) and produce ferric iron (Fe^{3+}) oxides. The fraction of Fe^{3+} oxides that is not used by anaerobic bacteria to remineralize organic matter settles to the seabed, forming iron deposits.

nutrient uptake during the glacial advance and in regions of open water, limited organic matter remineralization in a partly ice-covered ocean, and PO_4^{3-} adsorption onto iron oxides in an ocean with relatively high Fe^{2+} concentrations. Hence, we examined iron deposition patterns at 100%, 10%, 3% and 1% the mean present-day seawater $[PO_4^{3-}]$ (3 µM), the lower three of which are within the proposed range required to sustain low Proterozoic atmospheric O_2 levels[13,14], and consistent with low Proterozoic primary productivity[15]. With these parameter combinations, cases in which 90% or more of the iron deposited within the model grid points corresponding to the hydrothermal Fe^{2+} sources were considered less viable for BIF deposition on multiple continental margins, as suggested by the sedimentary record[10].

Our simulations show that the spatial pattern of Fe^{3+} precipitation is sensitive to both the extent of ice cover and the mean seawater $[PO_4^{3-}]$. To elucidate Fe^{3+} precipitation in a partially glaciated ocean, we consider the 12° S to 12° N ice-free ocean snowball with a mean $[PO_4^{3-}]$ of 3% modern levels. The flux of O_2 produced (via photosynthesis) in this snowball is limited due to both a low ice-free surface area and low PO_4^{3-} availability. This small amount of O_2 is distributed within the ocean by the circulation. However, the circulation in the juvenile, narrow ocean basins that were formed by the break-up of the supercontinent Rodinia is much weaker than in other regions (Supplementary Fig. 2). Since a hydrothermal source is also located within these poorly ventilated basins, they are a suitable site for accumulation and mobility of Fe^{2+}, which is oxidized at the 'chemical reaction and deposition fronts' in this region (Fig. 2a–f). The intersection of Fe^{2+}-bearing water and O_2-bearing water at these fronts produces Fe^{3+}, which is insoluble in seawater. The seawater insoluble Fe^{3+} sinks through the water column and a fraction of it is used by anaerobic bacteria to remineralize organic matter to replenish the marine PO_4^{3-} and Fe^{2+} pools, while the rest is deposited on the seafloor in the region. In contrast, we do not observe Fe^{2+} mobility around the hydrothermal vent located in the well-ventilated southeastern ocean and all the Fe^{2+} is oxidized (and precipitates) near the vent (Supplementary Fig. 3).

In partially ice-covered oceans with a mean $[PO_4^{3-}]$ that is 1–10% of today's, the distribution of model iron deposition rates (Fig. 3a,b and Supplementary Figs. 4g,h and 5e,f) away from the hydrothermal sources are within the range of estimated Sturtian BIF deposition rates (between ~0.003 and ~0.4 mol m^{-2} yr^{-1}; Supplementary Section 2). This model consistency with the observations is achieved at $[Fe^{2+}]$ approximately two orders of magnitude lower than previously thought to be required for widespread Neoproterozoic BIF deposition[16,17]. Thus, we suggest that Fe^{2+} supply and mobility, not concentration, are the actual requirements for widespread BIF deposition, in the Neoproterozoic and over Earth history in general. At modern mean seawater $[PO_4^{3-}]$, most of the ocean interior is oxygenated, and >95% of the iron precipitates near the hydrothermal Fe^{2+} sources.

Multiple BIF deposition sites emerge in the snowball simulations with 1–10% modern $[PO_4^{3-}]$ (Fig. 3a,b and Supplementary Figs. 4g,h and 5e,f), several of which are located in the deep ocean away from the continents. BIFs deposited at these deep sites are unlikely to be preserved, in contrast with the BIFs deposited on the continental margins facing the young ocean basins that formed during the break-up of Rodinia. This is consistent with the clustering of all but one of the BIFs dated to the Sturtian pan-glacial around these young ocean basins (Supplementary Fig. 6). The palaeogeographic reconstruction[18] does not resolve inland seas, which host some of the Neoproterozoic BIFs, but we postulate that iron deposition is expected also in such seas that were connected to the basins represented in the model (for example, apparent inland BIF locations in Fig. 3a,b). We assessed the agreement between iron deposition patterns obtained in different simulations with the spatial distribution of Neoproterozoic BIFs (Supplementary Section 3 and Supplementary Fig. 7). By and large, in simulations with mean seawater $[PO_4^{3-}]$ between 1% and 10% modern levels, O_2-bearing and Fe^{2+}-bearing water masses meet in the vicinity of Sturtian BIFs for the two partially ice-covered oceans considered. However, neither the ice-free ocean nor the partially ice-covered oceans show an affinity for precipitation of BIFs at modern $[PO_4^{3-}]$ levels, and all the Fe^{2+} is deposited close to the hydrothermal source. These results suggest that iron deposition patterns and rates consistent with the Sturtian BIFs can be obtained in partially ice-covered oceans with lower-than-present seawater $[PO_4^{3-}]$ (<~10% modern levels). Due to model uncertainties, we stop short of attempting to identify the precise $[PO_4^{3-}]$ levels and meridional ice extent that yield the most consistent iron deposition patterns.

To conclude, we contextualize our findings within the hard versus soft snowball debate. The hard snowball state[19–22] is suggested to have led to an anoxic ocean interior in which dissolved Fe^{2+} accumulated, to be oxidized and deposited only in spatially limited regions where O_2 was available, such as the interface between anoxic seawater and oxygenated meltwater plumes near the ice grounding line[10,23]. Under such a scenario, production of BIFs is expected on all glaciated continental margins[10], in contrast with the occurrence of Neoproterozoic BIFs only on some continental margins (Fig. 3a,b). However, fortuitous combinations of ice-sheet hydrology, meltwater residence times and subglacial bedrock geology may result in a distribution akin to the observed distribution of Sturtian BIFs even in a hard snowball. Our analysis shows that a phosphate-deficient ocean is conducive to production of BIFs for different extents of marine ice cover, wherever Fe^{2+}-bearing and oxygenated water masses meet. We find several combinations of $[PO_4^{3-}]$ and marine ice cover that predict BIF deposition at multiple sites, including on the continental margins facing the young ocean basins that formed during the fragmentation of Rodinia, consistent with the observed distribution of Sturtian BIFs (Fig. 3a,b and Supplementary Figs. 4g,h and 5e,f). The coarse resolution of our model and other limitations (for example, absence of a dynamic atmosphere–ice–ocean coupling, uncertainties in seafloor topography) prevent us from predicting the meridional extent of marine ice cover during the Neoproterozoic pan-glacials. Nevertheless, our findings prompt investigations of the plausibility of a soft snowball state in more complete climate models, which include atmosphere–ocean–cryosphere coupling and a realistic continental configuration. Lastly, our findings highlight the role of Fe^{2+} fluxes into, and mobility within, Earth's oceans as the necessary conditions for widespread BIF deposition. In contrast with previous suggestions, a high Fe^{2+} concentration is found unnecessary.

https://doi.org/10.1038/s41561-024-01406-4

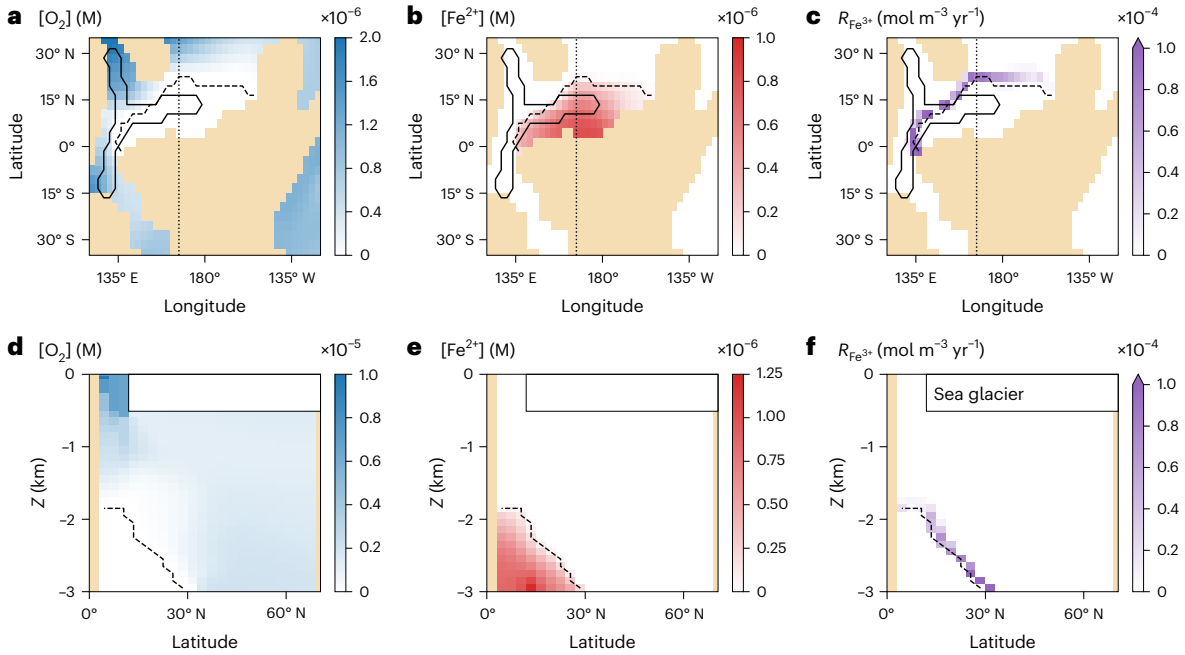

Fig. 2 | Results of the snowball simulation with 12° S to 12° N ice-free ocean and mean seawater phosphate concentration ($[PO_4^{3-}]$) of 0.1 µM (3% modern). Latitude–longitude cross-section at a depth of −2.5 km (top) and latitude–depth cross-section at 166.5° E (bottom) of oxygen ($[O_2]$) (**a**,**d**), ferrous iron ($[Fe^{2+}]$) (**b**,**e**) and ferric iron (Fe^{3+}) precipitation rate ($R_{Fe^{3+}}$) (**c**,**f**). The solid black contours in **a**–**c** mark the sites of hydrothermal Fe^{2+} injection, based on estimated locations of mid-oceanic ridges. The dashed black lines enclose the region where $[O_2] = 0$ and the 'chemical reaction front' is adjacent to it. The dotted line in the top panels mark the 166.5° E longitude; the latitude–depth cross sections in **d**–**f** are along this longitude. The light-brown shading in **a**–**c** indicates the approximate continental configuration during the Sturtian pan-glacial[18].

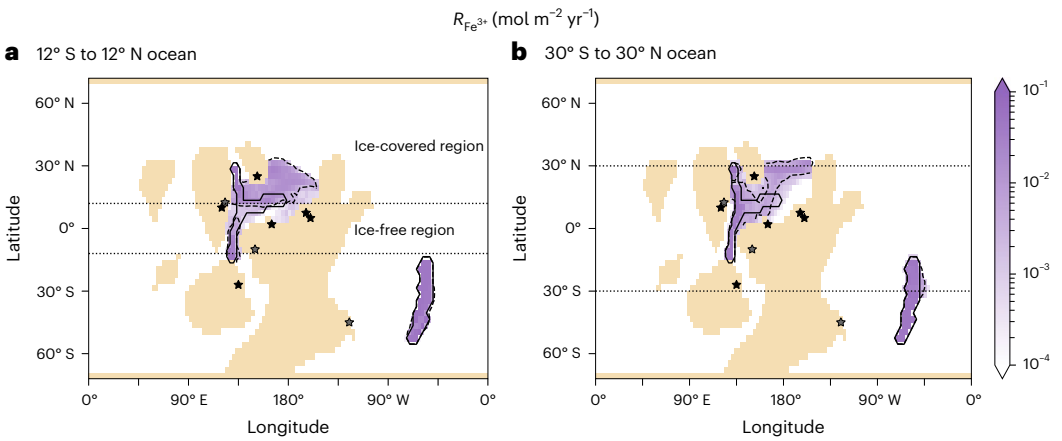

Fig. 3 | Iron deposition rates in the snowball simulation with 12° S to 12° N and 30° S to 30° N ice-free ocean; the mean seawater phosphate concentration ($[PO_4^{3-}]$) is 0.1 µM (3% modern). a,**b**, Spatial distribution of iron deposition rates ($R_{Fe^{3+}}$) in snowballs with an ice-free ocean between 12° S to 12° N (**a**) and 30° S to 30° N (**b**), respectively. Iron deposition rates are calculated by vertical integration of the profiles corresponding to net ferrous iron (Fe^{2+}) oxidation. The solid black contours mark the sites of hydrothermal Fe^{2+} injection, based on estimated locations of mid-oceanic ridges. The dotted black horizontal lines denote the extent of the ice-free region. The dashed black lines enclose the region where iron deposition rates are within the range estimated from Neoproterozoic BIFs. The stars indicate the approximate location of BIFs associated with the Sturtian pan-glacial. BIFs denoted by the grey stars have been excluded from the estimation of BIF deposition rate (Supplementary Section 2). The light-brown shading indicates the approximate continental configuration during the Sturtain pan-glacial.

Online content

Any methods, additional references, Nature Portfolio reporting summaries, source data, extended data, supplementary information, acknowledgements, peer review information; details of author contributions and competing interests; and statements of data and code availability are available at https://doi.org/10.1038/s41561-024-01406-4.

References

1. Bekker, A. et al. Iron formation: the sedimentary product of a complex interplay among mantle, tectonic, oceanic, and biospheric processes. *Econ. Geol.* **105**, 467–508 (2010).
2. Konhauser, K. O. et al. Iron formations: a global record of Neoarchaean to Palaeoproterozoic environmental history. *Earth Sci. Rev.* **172**, 140–177 (2017).
3. Lyons, T. W., Reinhard, C. T. & Planavsky, N. J. The rise of oxygen in Earth's early ocean and atmosphere. *Nature* **506**, 307–315 (2014).
4. Kirschvink, J. L. Late Proterozoic low-latitude global glaciation: the snowball Earth. *Proterozoic Biosphere* **52**, 51–52 (1992).
5. Hoffman, P. F., Kaufman, A. J., Halverson, G. P. & Schrag, D. P. A Neoproterozoic snowball Earth. *Science* **281**, 1342–1346 (1998).

6. Evans, D. A. D. Stratigraphic, geochronological, and paleomagnetic constraints upon the Neoproterozoic climatic paradox. *Am. J. Sci.* **300**, 347–433 (2000).
7. Hyde, W. T., Crowley, T. J., Baum, S. K. & Peltier, W. R. Neoproterozoic 'snowball Earth' simulations with a coupled climate/ice-sheet model. *Nature* **405**, 425–429 (2000).
8. Nelson, L. L. et al. Geochronological constraints on Neoproterozoic rifting and onset of the Marinoan glaciation from the Kingston Peak Formation in Death Valley, California (USA). *Geology* **48**, 1083–1087 (2020).
9. Rooney, A. D., Yang, C., Condon, D. J., Zhu, M. & Macdonald, F. A. U–Pb and Re–Os geochronology tracks stratigraphic condensation in the Sturtian snowball Earth aftermath. *Geology* **48**, 625–629 (2020).
10. Hoffman, P. F. et al. Snowball Earth climate dynamics and Cryogenian geology–geobiology. *Sci. Adv.* **3**, e1600983 (2017).
11. Abbot, D. S., Voigt, A. & Koll, D. The Jormungand global climate state and implications for Neoproterozoic glaciations. *J. Geophys. Res.* **116**, D18103 (2011).
12. Yang, J., Peltier, W. R. & Hu, Y. The Initiation of modern "soft snowball" and "hard snowball" climates in CCSM3. Part II: climate dynamic feedbacks. *J. Clim.* **25**, 2737–2754 (2012).
13. Laakso, T. A. & Schrag, D. P. Regulation of atmospheric oxygen during the Proterozoic. *Earth Planet. Sci. Lett.* **388**, 81–91 (2014).
14. Laakso, T. A. & Schrag, D. P. A theory of atmospheric oxygen. *Geobiology* **15**, 366–384 (2017).
15. Crockford, P. W. et al. Triple oxygen isotope evidence for limited mid-Proterozoic primary productivity. *Nature* **559**, 613–616 (2018).
16. Chan, C. S., Emerson, D. & Luther, G. W. The role of micro-aerophilic Fe-oxidizing micro-organisms in producing banded iron formations. *Geobiology* **14**, 509–528 (2016).
17. Song, H. et al. The onset of widespread marine red beds and the evolution of ferruginous oceans. *Nat. Commun.* **8**, 399 (2017).
18. Li, Z. X. et al. Assembly, configuration, and break-up history of Rodinia: a synthesis. *Precambrian Res.* **160**, 179–210 (2008).
19. Yang, J., Peltier, W. R. & Hu, Y. The initiation of modern soft and hard snowball Earth climates in CCSM4. *Climate* **8**, 907–918 (2012).
20. Ashkenazy, Y. et al. Dynamics of a snowball Earth ocean. *Nature* **495**, 90–93 (2013).
21. Ashkenazy, Y., Gildor, H., Losch, M. & Tziperman, E. Ocean circulation under globally glaciated snowball earth conditions: steady-state solutions. *J. Phys. Oceanogr.* **44**, 24–43 (2014).
22. Ashkenazy, Y. & Tziperman, E. Variability, instabilities, and eddies in a snowball ocean. *J. Clim.* **29**, 869–888 (2016).
23. Lechte, M. A. et al. Subglacial meltwater supported aerobic marine habitats during snowball Earth. *Proc. Natl Acad. Sci. USA* **116**, 25478–25483 (2019).

https://doi.org/10.1038/s41561-024-01406-4

Methods

Ocean

We use the Massachusetts Institute of Technology General Circulation Model (MITgcm)[24] to perform the simulations discussed in this study. The MITgcm is a free, open-source GCM in which a finite volume method is implemented to solve the equations of fluid motion (that is, momentum equations, continuity equation and diffusion equations of temperature and salinity and equation of state). We employ the full equation of state provided in the MITgcm, MDJWF[25], and make the hydrostatic and Boussinesq approximations. The model uses a spherical grid spanning 72° S to 72° N with a resolution of 3° in latitude and has 37 vertical levels spanning a depth of 3,000 m (height of vertical levels from the surface to the bottom: 10 m, 12 m, 16 m, 20 m, 25 m, 32 m, 40 m, 50 m, 60 m, 75 m, 80 m, 2 levels × 90 m, and 24 levels × 100 m). The longitudinal resolution is 3° as well, with 20 grid points in the idealized box configuration simulations and 120 grid points in the Neoproterozoic simulations. Unresolved eddies in the ocean are parameterized using the Gent-McWilliams/Redi (GM-Redi) scheme[26,27], and the background diffusion coefficient is set to 1,000 $m^2\,s^{-1}$. The lateral and vertical viscosities are set to $5\times10^5\,m^2\,s^{-1}$ and $10^{-3}\,m^2\,s^{-1}$, and the vertical diffusivity and implicit vertical diffusivity for convection are set to $10^{-4}\,m^2\,s^{-1}$ and $10\,m^2\,s^{-1}$. We also use a non-dimensional grid-dependent biharmonic viscosity of 0.1 to suppress the grid-scale noise. The vertical diffusivity for biogeochemical variables is set to $3\times10^{-5}\,m^2\,s^{-1}$. The third-order direct space-time flux limiter advection scheme (no. 33) is used for both momentum tracers and biogeochemical variables. The flat bathymetry ocean is subjected to a constant geothermal heat flux of 0.1 W m^{-2} (ref. 28). At the surface, the ocean is forced by a zonal wind stress that changes for the different meridional extent of the sea glaciers. The wind stress field for the idealized box configuration simulations is similar to the present-day, and for ice-free Neoproterozoic simulation is the zonally averaged wind stress obtained from fully coupled ocean–atmosphere simulation of Cambrian–Precambrian boundary[29]. The wind stress fields for our snowball simulation conditions (spatial grid and ice opening) are generated by setting the wind stress over the ice-covered region to zero and using zonally averaged wind stress profiles over the ice-free region that are based on results from simulations of partially glaciated climate states carried out on fully coupled GCMs[30,31]. The temperature at the surface ($z = 0$ m) is restored to temperature fields that are also generated on the basis of coupled model results[11,12]. Supplementary Fig. 8a,b shows the zonally averaged restoration temperature and wind stress over the ocean for different meridional extents of sea glaciers. Supplementary Fig. 8c shows the evaporation minus precipitation (E − P) fields over the ocean in the box simulations and in the Neoproterozoic ice-free simulations, these idealized E − P fields are generated by introducing a small asymmetry to the E − P field described in ref. 32. In both the snowballs, melting under the sea glaciers is balanced by evaporation in the ice-free region, which conserves the mean salinity of the ocean.

Sea glaciers

Given the uncertainties regarding the thickness of ice during the Neoproterozoic glaciations, we estimate ice thickness using a simplified energy balance. A similar calculation has been used to estimate the thickness of ice on Jupiter's moon Europa[33]. We begin by assuming that a constant geothermal flux of 0.1 W m^{-2} is applied to the ocean bottom and that the component of tidal heating in both the ice and ocean is negligible. Moreover, the temperature within the ice varies linearly with depth. In this case, the thickness of ice is given by

$$h = \rho_i c_{p,i} \kappa \frac{T_f - T_i}{Q}, \tag{1}$$

where ρ_i is the density, $c_{p,i}$ is the heat capacity and κ is the temperature diffusion constant of ice. T_f and T_i are the freezing and surface temperature of the ice, and Q is the internal heat flux (the geothermal heat flux). T_f is a function of salinity and pressure:

$$T_f = 273.16 + 0.0901 - 0.0575 \times S - 7.61 \times 10^{-8} \times P_b, \tag{2}$$

where S is the salinity and $P_b = \rho g h$ is the pressure at the bottom of the ice. The gradient in solar insolation yields a gradient in the surface temperature of the ice, and in turn, a gradient in ice thickness. This gradient in ice thickness causes it to flow smoothly, thereby partially relaxing the gradient[34]. Hence, we approximate the thickness of the ice as the meridional average of h calculated using the prescribed temperature field. Under these assumptions, the ice thickness can iteratively be estimated as:

$$\langle h \rangle_{j+1} = \rho_i c_{p,i} \kappa \frac{\langle T_f \rangle_j - \langle T_i \rangle}{Q}. \tag{3}$$

The algorithm[33], when initialized from the typical seawater freezing temperature of 271 K and the surface temperature fields such as the ones given in refs. 11,12, predicts a certain ice thickness, which implies a certain P_b value and a modified freezing temperature. For the temperature fields shown in Supplementary Fig. 8a, the ice thickness converges to 490 m and 253 m below the sea surface within a few iterations for snowballs with 12° S to 12° N ice-free ocean and 30° S to 30° N ice-free ocean, respectively. To avoid any numerical artefacts that may arise from partially filled grid cells, we use a thickness of 510 m and 265 m below the sea surface for the snowballs with 12° S to 12° N ocean and 30° S to 30° N ocean, respectively. The effect of this sea glacier is simulated using the SHELFICE package[35]. Unlike the SEAICE package, the SHELFICE package in the MITgcm can handle a thick sea glacier spanning over multiple vertical levels, which makes it better suited to snowball Earth modelling.

Biogeochemical cycle

The biogeochemical model presented here is based on refs. 36,37, implemented in the MITgcm using a combination of the GCHEM and DIC packages[38]. MITgcm's biogeochemical setup (GCHEM + DIC), in its default configuration, considers coupled cycles of carbon, oxygen, phosphorus and alkalinity. These cycles are expressed using five variables that do not affect the physical circulation: dissolved inorganic carbon (DIC), alkalinity (Alk), phosphate (PO_4^{3-}), dissolved organic phosphorus (DOP) and oxygen (O_2). The velocity fields and eddy diffusivities calculated by the physical model are used to transport these compounds, which are additionally produced and consumed locally by biogeochemical reactions, as described below.

For this study, we focus on the phosphorus and oxygen cycles. Additionally, we incorporate an iron (Fe^{2+}) cycle and a well-mixed atmospheric box to the pre-existing setup. The atmospheric box only keeps track of the total O_2 in the atmosphere. The values of all parameters described below are provided in Supplementary Table 1. The sources and sinks for each tracer are summarized below:

$$\frac{\partial}{\partial t}\left[PO_4^{3-}\right] = -J_{\text{production}} - \frac{\partial}{\partial z}F_P + \kappa_{\text{remin}}\left[DOP\right], \tag{4}$$

$$\frac{\partial}{\partial t}\left[DOP\right] = f_{DOP} J_{\text{production}} - \kappa_{\text{remin}}\left[DOP\right], \tag{5}$$

$$\begin{aligned}\frac{\partial}{\partial t}\left[O_2\right] = {} & \frac{k_w}{\Delta z_{\text{surf}}}\left(\frac{n_{O_2}^{\text{model atmosphere}}}{n_{O_2}^{\text{present day}}}\left[O_2\right]_{sat} - \left[O_2\right]_{\text{surf}}\right) \\ & + f(\left[O_2\right]) \times \left(r_{O_2:P}\frac{\partial}{\partial t}\left[PO_4^{3-}\right]\right) - k_{Fe}\left[Fe^{2+}\right],\end{aligned} \tag{6}$$

$$\frac{\partial}{\partial t}\left[Fe^{2+}\right] = F_{Fe}^{\text{hydrothermal}} - k_{Fe}\left[Fe^{2+}\right] - \frac{\partial}{\partial z}F_{Fe}^{\text{recycle}}, \tag{7}$$

where square brackets denote concentration, $J_{\text{production}}$ is primary production. During production, a fraction of PO_4^{3-} utilized by phytoplankton is converted to DOP (f_{DOP}) and the rest ($1-f_{\text{DOP}}$) is converted to particulate organic phosphorus (POP); κ_{remin} is the rate constant of remineralization of DOP to PO_4^{3-} and $\frac{\partial}{\partial z}F_{\text{P}}$ is the partial derivative with depth of the POP sinking flux that is remineralized at different rates during aerobic and anaerobic respiration (see below). The gas transfer velocity for O_2 is given by k_w, and Δz_{surf} is the thickness of the surface layer. The moles of O_2 in the model atmosphere and the present-day atmosphere are given by $n_{O_2}^{\text{model atmosphere}}$ and $n_{O_2}^{\text{present day}}$ respectively, and $[O_2]_{\text{sat}}$ and $[O_2]_{\text{surf}}$ are the saturation and surface concentration of O_2, respectively. The function $f([O_2])=1$ for $[O_2]>0$ and 0 otherwise. The number of moles of O_2 consumed to remineralize 1 mole of the typical Neoproterozoic marine biomass is given by $-r_{O_2:P}$ (see below).

$F_{\text{Fe}}^{\text{hydrothermal}}$ is the hydrothermal influx of Fe^{2+} to the ocean, k_{Fe} is the oxidation rate of Fe^{2+} to Fe^{3+}, which accounts for both abiotic and microbial pathways (described below), and $\frac{\partial}{\partial z}F_{\text{Fe}}^{\text{recycle}}$ is the partial derivative with depth of the particulate Fe^{3+} sinking flux, which gives the rate at which particulate Fe^{3+} is recycled back to Fe^{2+} by anaerobic remineralization of organic matter. The tendency term for the number of moles of O_2 in the model atmosphere is

$$\frac{\mathrm{d}}{\mathrm{d}t}n_{O_2}^{\text{model atmosphere}} = -\xi\left(k_w A_{\text{surf}}\left(\frac{n_{O_2}^{\text{model atmosphere}}}{n_{O_2}^{\text{present day}}}[O_2]_{\text{sat}}-[O_2]_{\text{surf}}\right)-\Phi_{\text{red}}\right), \tag{8}$$

where $\xi=10^4$ is an arbitrary constant introduced to accelerate the convergence of the atmospheric box to a steady state, A_{surf} is the area of the ocean surface, Φ_{red} is the (mole equivalent) rate of consumption of O_2 required to balance the volcanic flux of reduced gases into the atmosphere (for example, SO_2, H_2S, CO, CH_4 and H_2). Other oxygen sinks relevant to the present-day Earth system, like oxidative weathering of the continents and respiration by the terrestrial biosphere, are considered negligible during a global glaciation.

$J_{\text{production}}$, which is a function of the light (L) and $\left[PO_4^{3-}\right]$, is given by

$$J_{\text{production}} = \alpha\frac{L}{L+\kappa_L}\frac{\left[PO_4^{3-}\right]}{\left[PO_4^{3-}\right]+\kappa_{PO_4^{3-}}}, \tag{9}$$

where κ_L and $\kappa_{PO_4^{3-}}$ are Michaelis–Menten-type half-saturation constants typical of ocean biology, and α is the maximum community production. The expression for L is

$$L = f_{\text{PAR}}Q_{\text{SW}}\times\exp(-kz), \tag{10}$$

where f_{PAR} is the fraction of shortwave radiation (SW) available for photosynthesis and k is the light attenuation constant. Since the light available for photosynthesis declines exponentially with depth, most of the biological activity in the ocean is close to the surface. Recall that primary production converts a fraction of PO_4^{3-} to DOP (f_{DOP}), which can be advected by the physical circulation in the ocean, while the rest is POP, which sinks[39]. The downwards sinking flux of POP is given by

$$F_{\text{POP}} = \begin{cases}(1-f_{\text{DOP}})\int_0^{z_i}J_{\text{production}}\,\mathrm{d}z \text{ if } z<z_c\\ (1-f_{\text{DOP}})\int_0^{z_c}J_{\text{production}}\,\mathrm{d}z \text{ if } z\geq z_c\end{cases}, \tag{11}$$

where z_i is a reference depth below which the downwards flux of POP is calculated and z_c is the compensation depth. In present-day ocean models, POP is remineralized according to a power law relation related almost entirely to aerobic respiration[40]. Additionally, our model accounts for remineralization of POP by anaerobic microbes that reduce Fe^{3+} particles (see below).

As was previously mentioned, Fe^{2+} in the ocean can be oxidized by abiotic and microbial pathways, both O_2-related and light driven. The Fe^{2+} oxidation rate accounting for both abiotic and microbial processes is

$$k_{\text{Fe}} = \frac{k_{\text{Fe}}^{\text{ab}}}{1-f_{\text{bio}}}, \tag{12}$$

where $k_{\text{Fe}}^{\text{ab}}$ is the abiotic rate constant of oxidation and f_{bio} is the fraction of microbial Fe^{2+} oxidation out of the total oxidation as a function of available $[O_2]$ (ref. 41); $k_{\text{Fe}}^{\text{ab}}$ is given by

$$k_{\text{Fe}}^{\text{ab}} = k_1[O_2]\left[OH^-\right]^2$$

$$\log k_1 = 21.56-\frac{1{,}545}{T}-3.29\sqrt{I}+1.52I, \tag{13}$$

where T is the temperature (in kelvin), $I=\frac{19.992S}{10^3-1.005S}$ and S is the salinity of seawater[42]. The fraction of microbial Fe^{2+} oxidation is given by

$$f_{\text{bio}} = 1.074\times10^{-3}\times\exp\left(-3.446\log\left(\frac{[O_2]}{K_H}\right)\right), \tag{14}$$

where K_H is Henry's law constant for O_2:

$$K_H = 1.3\times10^{-3}\times\exp\left(1{,}500\left(\frac{1}{T}-\frac{1}{298.15}\right)\right). \tag{15}$$

f_{bio} is capped at 0.95, an upper bound based on experimental results[41]. To allow model timesteps that are long enough so that convergence is reached over reasonable runtimes, chemical rate constants could not be too large. Thus, we prescribed an upper limit on k_{Fe} of $10^{-5}\,\text{s}^{-1}$. This upper limit was applied wherever O_2 concentrations were high enough to result in k_{Fe} that was too large to allow efficient model timesteps, typically in the well-oxygenated regions in the ocean (for example, near the surface in the snowball with 12° S to 12° N ocean). The upper limit of k_{Fe} was prescribed in ~68% of the ocean volume in the snowball simulation with 12° S to 12° N ocean with 1% modern $[PO_4^{3-}]$, in >90% of the ocean volume for a lower ice cover or higher $[PO_4^{3-}]$. The model results were relatively insensitive to this choice of an upper limit on k_{Fe} (Supplementary Fig. 9).

The downwards flux of Fe^{3+} produced from oxidation of Fe^{2+} is given by

$$F_{\text{Fe}}^{\text{down}} = \int_0^{z_u}k_{\text{Fe}}[Fe^{2+}]\mathrm{d}z, \tag{16}$$

where z_u is the reference up to which the downwards flux of Fe^{3+} is calculated. We assume that a fraction of sinking Fe^{3+} is preserved ($f_{\text{preserved}}$) while the rest is remineralized by anaerobic microbes. This process restores some Fe^{2+} and is summarized by the following reaction:

$$4Fe^{3+}+CH_2O+5OH^-\rightarrow 4Fe^{2+}+HCO_3^-+3H_2O.$$

The anaerobic reduction of Fe^{3+} by bacteria follows Michaelis–Menten-type kinetics with respect to the concentrations of both organic matter and Fe^{3+}:

$$\frac{d}{dt}\left[Fe^{3+}\right] = \mu\min\left(\frac{[Fe^{3+}]}{\kappa_{\text{Fe}}+[Fe^{3+}]},\frac{[C]}{\kappa_C+[C]}\right), \tag{17}$$

where μ is the typical respiration rate, and $[Fe^{3+}]$ and [C] are the concentrations of Fe^{3+} and organic matter, respectively. The relevant half-saturation constants for Fe^{3+} and C are κ_{Fe} and κ_C, respectively, and the smaller of the saturation terms is considered to limit the Fe^{3+} reduction rate. Assuming a typical C:P ratio of 100:1 yields

$$\frac{\mathrm{d}}{\mathrm{d}t}\left[Fe^{3+}\right] = \mu \min\left(\frac{\left[Fe^{3+}\right]}{\kappa_{Fe} + \left[Fe^{3+}\right]}, \frac{[POP]}{\frac{\kappa_C}{100} + [POP]}\right), \quad (18)$$

and

$$\frac{\mathrm{d}}{\mathrm{d}t}[POP] = \frac{\mu}{400} \min\left(\frac{\left[Fe^{3+}\right]}{\kappa_{Fe} + \left[Fe^{3+}\right]}, \frac{[POP]}{\frac{\kappa_C}{100} + [POP]}\right). \quad (19)$$

The factor of 400 comes from the Fe:C:P stoichiometry of the reaction. To calculate the flux of recycled Fe^{3+} ($F_{Fe}^{recycle}$) and the effect of Fe^{3+} reduction on the vertical POP remineralization profile, we further assume that [POP] and $[Fe^{3+}]$ are proportional to F_P and F_{Fe}^{down} respectively. If $F_{Fe}^{down} > (F_P/400)$, the fluxes of recycled Fe^{3+} and POP are given by:

$$F_P(z) = \begin{cases} F_{POP}\left(\frac{z}{z_i}\right)^{-\left(a_{remin} + \frac{\mu}{4\kappa_C \times a}\right)} \text{ if } F_P < w(z)(\kappa_C/100) \\ F_{POP}\left(\frac{z}{z_i}\right)^{-a_{remin}} \text{ otherwise} \end{cases}, \quad (20)$$

and

$$F_{Fe}^{recycle}(z) = (1 - f_{preserved}) F_{Fe}^{down} - \mu \frac{F_P(z)}{w(z)(\kappa_C/100) + F_P(z)}. \quad (21)$$

Similarly, when $F_{Fe}^{down} < (F_P/400)$, the fluxes of recycled Fe^{3+} and POP are given by

$$F_P(z) = F_{POP}\left(\frac{z}{z_i}\right)^{-a_{remin}}, \quad (22)$$

and

$$F_{Fe}^{recycle}(z) = \begin{cases} (1 - f_{preserved}) F_{Fe}^{down}\left(\frac{z}{z_i}\right)^{-\frac{\mu}{a\kappa_{Fe}}} \text{ if } F_{Fe}^{down} < w(z)\kappa_{Fe} \\ (1 - f_{preserved}) F_{Fe}^{down} \text{ otherwise} \end{cases}. \quad (23)$$

Here z_i is a reference depth below which the downwards flux of POP is calculated (note that $z_i = z_c$ when $z > z_c$), a is the vertical gradient of particle sinking velocity such that $w(z) = az$ yields the speed of the sinking particles at depth z, and a_{remin} is the exponent in Martin's curve for POP remineralization in the modern ocean. Note that even though F_P and F_{POP} have the same units, the quantities are not the same. F_{POP} is the depth-dependent downwards sinking flux of POP. On the other hand, F_P is the depth-dependent POP remineralization flux, which can change based on whether remineralization of organic matter is anaerobic or aerobic.

The Fe^{2+} influx to the ocean from axial and off-axis hydrothermal circulation depends on the Fe^{2+} concentration in the fluid and the total water fluxes. The concentration of Fe^{2+} in axial and off-axis hydrothermal fluids is estimated to be in the range $(0.75–6.5) \times 10^{-3}$ mol kg^{-1} and $(0.4–6.0) \times 10^{-6}$) mol kg^{-1}, respectively[43–45]. Assuming that the Fe^{2+} concentration is uniformly distributed in these ranges and the axial and off-axis water fluxes follow the distributions shown in ref. 46, we generated probability distributions corresponding to the axial and off-axis influx of hydrothermal Fe^{2+} to the ocean (Supplementary Fig. 10a,b). Separate from hydrothermal Fe^{2+} fluxes, weathering of seafloor basalt can deliver Fe^{2+} to the ocean[47,48]. The Fe^{2+} flux from seafloor weathering is rather difficult to constrain in the well-oxygenated modern ocean but it is estimated to be ~0.1–0.3 Tmol yr^{-1} and as high as 1.0 Tmol yr^{-1} (ref. 49), though it is unclear that all the Fe^{2+} lost from the basalt actually reaches the ocean. Given the existing estimates, we adopt a weathering Fe^{2+} flux uniformly distributed between 0.1 and 0.3 Tmol yr^{-1} (Supplementary Fig. 10c).

Convolving the distributions of axial and off-axis hydrothermal fluxes and seafloor weathering flux yields a range of Fe^{2+} influxes between 0.2 and 0.67 Tmol yr^{-1} (95% confidence interval) with a mode of 0.36 Tmol yr^{-1} (Supplementary Fig. 10d). Though some have suggested higher hydrothermal fluxes in Earth's deep past due to higher radiogenic heat production in the mantle[50], it remains unclear whether the higher heat production led instead to more sluggish seafloor spreading[51] and a hydrothermal flux like the Phanerozoic. We do not upscale the hydrothermal water flux, leading to conservatively low Fe^{2+} influx estimates. Following the above analysis, we distribute the mode Fe^{2+} influx of 0.36 Tmol yr^{-1} on the model grid points corresponding to the suggested locations of seafloor spreading centres during the Sturtian glaciation. Moreover, we do not taper the Fe^{2+} influx with increasing distance from the spreading centres, since both near-axis and off-axis hydrothermal inputs occur close to the spreading centres (considering the spatial resolution of the ocean model), and the dissolved products of seafloor weathering are expected to reach the ocean mostly where the sedimentary cover on the basaltic crust is thin to absent (that is, near the spreading centres).

The marine phytoplankton community during the Neoproterozoic primarily composed of cyanobacteria. Previous studies[52–55] show that the metabolite content of typical cyanobacterial biomass is 51% protein, 16% carbohydrates, 23% lipid and 10% nucleic acid, which is slightly different from the average composition of modern phytoplankton (which includes diatoms, coccolithophores, dinoflagellates and cyanobacteria): 54% protein, 26% carbohydrates, 16% lipid and 4% nucleic acid[56]. Despite these differences in the metabolite content, the oxidation state of cyanobacterial biomass is not substantially different from the gross modern assemblage (we estimated <1% variation in $H:C_{org}$ and <10% variation in $O:C_{org}$ ratios), which suggests that the difference between the Neoproterozoic and present-day O_2:P ratio is expected to arise from a difference between the C:P ratios of cyanobacteria and the modern assemblage and not from the difference in the carbon oxidation state. Using the mean C:N:P ratio of 152:25:1 for cyanobacteria[57], we calculate the following elemental composition of typical Neoproterozoic plankton: $C_{152}H_{247}O_{61}N_{25}P$. As per this mean composition, the $r_{O_2:P}$ ratio is estimated to be −216, which is ~45% more negative than its present-day value of −150 (ref. 56). In other words, 45% more O_2 is consumed per mole of organic phosphorus liberated during organic matter remineralization.

As mentioned above, the majority of O_2 sinks on the present-day Earth were negligible during the Neoproterozoic snowball Earth events. However, reducing volcanic emissions (SO_2, H_2S, CO, CH_4 and H_2) can be an important sink for O_2 in a globally glaciated climate (Supplementary Table 2). All listed fluxes are approximate but can be used to reasonably estimate the equivalent moles of O_2 consumed annually by oxidation of the reduced gases.

Data availability

The model data and the Python script necessary to reproduce the figures presented in this study are available from the figshare repository at https://doi.org/10.6084/m9.figshare.25130783.v1 (ref. 58). The other data that have been analysed can be accessed through the links provided in the studies that have been cited.

Code availability

The simulations are carried out using the MITgcm, an open-source ocean model that can be downloaded from https://mitgcm.readthedocs.io/en/latest/overview/overview.html. The specific model configuration is available upon request.

References

24. Marshall, J., Adcroft, A., Hill, C., Perelman, L. & Heisey, C. A finite-volume, incompressible Navier Stokes model for studies of the ocean on parallel computers. *J. Geophys. Res. Oceans* **102**, 5753–5766 (1997).

25. McDougall, T. J., Jackett, D. R., Wright, D. G. & Feistel, R. Accurate and computationally efficient algorithms for potential temperature and density of seawater. *J. Atmos. Ocean Technol.* **20**, 730–741 (2003).
26. Redi, M. H. Oceanic isopycnal mixing by coordinate rotation. *J. Phys. Oceanogr.* **12**, 1154–1158 (1982).
27. Gent, P. R. & Mcwilliams, J. C. Isopycnal mixing in ocean circulation models. *J. Phys. Oceanogr.* **20**, 150–155 (1990).
28. Pollack, H. N., Hurter, S. J. & Johnson, J. R. Heat flow from the Earth's interior: analysis of the global data set. *Rev. Geophys.* **31**, 267–280 (1993).
29. Valdes, P. J., Scotese, C. R. & Lunt, D. J. Deep ocean temperatures through time. *Climate* **17**, 1483–1506 (2021).
30. Liu, Y., Peltier, W. R., Yang, J. & Vettoretti, G. The initiation of Neoproterozoic "snowball" climates in CCSM3: the influence of paleocontinental configuration. *Climate* **9**, 2555–2577 (2013).
31. Zhao, Z., Liu, Y. & Dai, H. Sea-glacier retreating rate and climate evolution during the marine deglaciation of a snowball Earth. *Glob. Planet. Change* **215**, 103877 (2022).
32. Ashkenazy, Y. & Tziperman, E. A wind-induced thermohaline circulation hysteresis and millennial variability regimes. *J. Phys. Oceanogr.* **37**, 2446–2457 (2007).
33. Ashkenazy, Y. The surface temperature of Europa. *Heliyon* **5**, e01908 (2019).
34. Ashkenazy, Y., Sayag, R. & Tziperman, E. Dynamics of the global meridional ice flow of Europa's icy shell. *Nat. Astron.* **2**, 43–49 (2017).
35. Losch, M. Modeling ice shelf cavities in a *z* coordinate ocean general circulation model. *J. Geophys. Res. Oceans* **113**, C08043 (2008).
36. McKinley, G. A., Follows, M. J. & Marshall, J. Mechanisms of air–sea CO_2 flux variability in the equatorial Pacific and the North Atlantic. *Glob. Biogeochem. Cycles* **18**, 1–14 (2004).
37. Dutkiewicz, S., Sokolov, A. P., Scott, J. & Stone, P. H. *A Three-Dimensional Ocean-Seaice-Carbon Cycle Model and Its Coupling to a Two-Dimensional Atmospheric Model: Uses in Climate Change Studies. Joint Program Report Series Report* (Massachusetts Institute of Technology, 2005).
38. MITgcm contributors. Biogeochemistry packages. *MITgcm* https://mitgcm.readthedocs.io/en/latest/phys_pkgs/phys_pkgs.html#biogeochemistry-packages (2019).
39. Yamanaka, Y. & Tajika, E. Role of dissolved organic matter in the marine biogeochemical cycle: studies using an ocean biogeochemical general circulation model. *Glob. Biogeochem. Cycles* **11**, 599–612 (1997).
40. Martin, J. H., Knauer, G. A., Karl, D. M. & Broenkow, W. W. VERTEX: carbon cycling in the northeast Pacific. *Deep Sea Res. Part A* **34**, 267–285 (1987).
41. Halevy, I., Alesker, M., Schuster, E. M., Popovitz-Biro, R. & Feldman, Y. A key role for green rust in the Precambrian oceans and the genesis of iron formations. *Nat. Geosci.* **10**, 135–139 (2017).
42. Millero, F. J., Sotolongo, S. & Izaguirre, M. The oxidation kinetics of Fe(II) in seawater. *Geochim. Cosmochim. Acta* **51**, 793–801 (1987).
43. Komada, T. et al. Dissolved organic carbon dynamics in anaerobic sediments of the Santa Monica Basin. *Geochim. Cosmochim. Acta* **110**, 253–273 (2013).
44. Mottl, M. J. et al. Warm springs discovered on 3.5 Ma oceanic crust, eastern flank of the Juan de Fuca Ridge. *Geology* **26**, 51 (1998).
45. Elderfield, H. & Schultz, A. Mid-ocean ridge hydrothermal fluxes and the chemical composition of the ocean. *Annu Rev. Earth Planet Sci.* **24**, 191–224 (1996).
46. Halevy, I. & Bachan, A. The geologic history of seawater pH. *Science* **355**, 1069–1071 (2017).
47. Poulton, S. W. & Raiswell, R. The low-temperature geochemical cycle of iron: from continental fluxes to marine sediment deposition. *Am. J. Sci.* **302**, 774–805 (2002).
48. Wolery, T. J. & Sleep, N. H. Hydrothermal circulation and geochemical flux at mid-ocean ridges. *J. Geol.* **84**, 249–275 (1976).
49. Hart, R. A. A model for chemical exchange in the basalt–seawater system of oceanic layer II. *Can. J. Earth Sci.* **10**, 799–816 (1973).
50. Thompson, K. J. et al. Photoferrotrophy, deposition of banded iron formations, and methane production in Archean oceans. *Sci. Adv.* **5**, eaav2869 (2019).
51. Korenaga, J. in *Archean Geodynamics and Environments* (eds Benn, K. Mareschal, J.-C. & Condie, K. C.) 7–32 (American Geophysical Union, 2006).
52. Molina, E., Martínez, M. E., Sánchez, S., García, F. & Contreras, A. Growth and biochemical composition with emphasis on the fatty acids of *Tetraselmis* sp. *Appl. Microbiol. Biotechnol.* **36**, 21–25 (1991).
53. Fábregas, J., Patiño, M., Vecino, E., Cházaro, F. & Otero, A. Productivity and biochemical composition of cyclostat cultures of the marine microalga *Tetraselmis suecica*. *Appl. Microbiol. Biotechnol.* **43**, 617–621 (1995).
54. Tahiri, M., Benider, A., Belkoura, M. & Dauta, A. Caractérisation biochimique de l'algue verte *Scenedesmus abundans*: influence des conditions de culture. *Ann. Limnol.* **36**, 3–12 (2000).
55. Viegas, C. V. et al. Algal products beyond lipids: comprehensive characterization of different products in direct saponification of green alga *Chlorella* sp. *Algal Res.* **11**, 156–164 (2015).
56. Anderson, L. A. On the hydrogen and oxygen content of marine phytoplankton. *Deep Sea Res. Part I* **42**, 1675–1680 (1995).
57. Sharoni, S. & Halevy, I. Geologic controls on phytoplankton elemental composition. *Proc. Natl Acad. Sci. USA* **119**, e2113263118 (2022).
58. Gianchandani, K. Dataset for "Production of Neoproterozoic banded iron formations in a partially ice-covered ocean" by Gianchandani et al. *figshare* https://doi.org/10.6084/m9.figshare.25130783.v1 (2024).

Acknowledgements

K.G., H.G. and Y.A. acknowledge the Joint National Natural Science Foundation of China, Israel Science Foundation Research Grant No. 2547/17 and the US-Israel Binational Science Foundation (BSF) Grant No. 2018152. I.H. acknowledges a Starting Grant from the European Research Council (OOID No. 755053). E.T. acknowledges NSF grant 2303486 from the P4CLIMATE programme and DOE grant DE-SC0023134. E.T. also thanks the Weizmann Institute for its hospitality during parts of this work.

Author contributions

K.G. led the conceptualization, method development, data curation and analysis, and code development and performed the numerical simulations presented in this study. I.H., H.G., Y.A. and E.T. contributed to the conceptualization, method development, supervision and validation of the study. H.G. and Y.A. additionally contributed to project administration, resource management and funding acquisition. Y.A. additionally was involved in software development. K.G. drafted the initial manuscript, and all the authors contributed to the text and participated in the review and approval of the final manuscript.

Competing interests

The authors declare no competing interests.

Additional information

Supplementary information The online version contains supplementary material available at https://doi.org/10.1038/s41561-024-01406-4.

Correspondence and requests for materials should be addressed to Kaushal Gianchandani or Itay Halevy.

Peer review information *Nature Geoscience* thanks Maxwell Lechte and Lennart Ramme for their contribution to the peer review of this work. Primary Handling Editor(s): James Super, in collaboration with the *Nature Geoscience* team.